Microcomputed Tomography for the Microstructure Evaluation of 3D Bioprinted Scaffolds

Salma P. Ramirez, Ivana Hernandez, Hannia V. Balcorta, Piyush Kumar, Vinod Kumar, Wilson Poon,* and Binata Joddar*

Cite This: https://doi.org/10.1021/acsabm.3c00621

Read Online

ACCESS | Metrics & More | Article Recommendations | Supporting Information

ABSTRACT: This study implemented the application of micro-computed tomography (micro-CT) as a characterization technique for the study and investigation of the microstructure of 3D scaffold structures produced via three-dimensional bioprinting (3DBP). The study focused on the preparation, characterization, and cytotoxicity analysis of gold nanoparticles (Au-NPs) incorporated into 3DBP hydrogels for micro-CT evaluation. The Au-NPs were characterized by using various techniques, including UV–vis spectrometry, dynamic light scattering (DLS), zeta potential measurement, and transmission electron microscopy (TEM). The characterization results confirmed the successful coating of the Au-NPs with 2 kDa methoxy-PEG and revealed their spherical shape with a mean core diameter of 66 nm. Cytotoxicity analysis using live–dead fluorescent microscopy indicated that all tested Au-NP solutions were nontoxic to AC16 cardiomyocytes in both 2D and 3D culture conditions. Scanning electron microscopy (SEM) showed distinguishable differences in image contrast and intensity between samples with and without Au-NPs, with high concentrations of Au-NPs displaying nanoparticle aggregates. Micro-CT imaging demonstrated that scaffolds containing Au-NPs depicted enhanced imaging resolution and quality, allowing for visualization of the microstructure. The 3D reconstruction of scaffold structures from micro-CT imaging using Dragonfly software further supported the improved visualization. Mechanical analysis revealed that the addition of Au-NPs enhanced the mechanical properties of acellular scaffolds, including their elastic moduli and complex viscosity, but the presence of cells led to biodegradation and reduced mechanical strength. These findings highlight the successful preparation and characterization of Au-NPs, their nontoxic nature in both 2D and 3D culture conditions, their influence on imaging quality, and the impact on the mechanical properties of 3D-printed hydrogels. These results contribute to the development of functional and biocompatible materials for tissue engineering and regenerative medicine applications.

KEYWORDS: 3D bioprinting, alginate-gelatin hydrogels, gold nanoparticles, micro-CT imaging, microstructure evaluation, mechanical properties
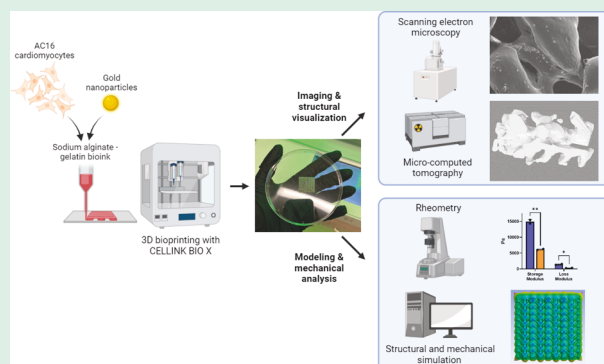
1. INTRODUCTION

The main objective of tissue engineering is the promotion of tissue repair or regeneration by using a combination of scaffolds with viable cells and biomolecules to create 3D tissues in vitro that can recapitulate all aspects of living tissues in vivo. As such, the design and development of scaffolds that can promote and enhance these goals are extremely important for the design of this process. Utilizing three-dimensional bioprinting (3DBP) technologies, cell scaffolds can be produced with a high degree of complexity, precision, and a resultant internal/core microstructure that can mimic the architecture of the native tissue extracellular matrix (ECM) present in vivo.[1] This is indeed critical as the scaffolds need to possess high pore interconnectivity to allow cells to distribute, attach, and grow in the structure. Nevertheless, the design and development of a scaffold microstructure that mimics the

native tissue architecture appropriately are challenging. Furthermore, there are inherent drawbacks to the process of 3DBP including nonhomogenous pore distribution throughout the scaffold, which can affect encapsulated cell viability and function.[2]

Therefore, a characterization technique that allows for the study of the microstructure of the 3DBP scaffolds is required to promote scale-up toward futuristic biomanufacturing. Advanced high-resolution imaging techniques such as micro-

computed tomography (micro-CT) can provide imaging capabilities with isotropic resolutions that range from 100 nm to a few millimeters, which may be critical when imaging a thick cell scaffold.[3] However, cell-based hydrogel scaffolds are composed of more than 70% aqueous environments, which makes their imaging challenging via this technique. We hypothesized that the micro-CT technique when applied for imaging of scaffolds embedded with contrast agents such as gold nanoparticles (Au-NPs) can provide higher contrast and resolution that is needed for studying the microstructure of the cell-based scaffold in order to predict its mechanical properties and biodegradability for tissue engineering applications.[4] The objectives of this study were to determine the optimized concentration of Au-NPs to be integrated into the 3DBP scaffolds to sustain cell growth and promote tissue regeneration while providing sufficient contrast for high resolution microscopic imaging; to utilize micro-CT scanning to explore the microstructure of 3DBP alginate-gelatin scaffolds incorporated with varying concentrations of Au-NPs; and to characterize as well as model the scaffold's mechanical properties. Herein, our goal was to elucidate the optimum concentration of Au-NPs for encapsulation within 3DBP hydrogel-based scaffolds that would allow both adequate contrast enhancement in micro-CT scanning and sustained biocompatibility of the encapsulated cells. Furthermore, this study also compared the scaffold's microstructure and mechanical properties via experimental and modeling techniques.

By applying micro-CT imaging of cell-based scaffolds, we will achieve a transformative breakthrough to quickly adapt to the fast-moving pace of biomanufacturing of engineered tissues and create new knowledge and research products in this field. Results from this study will help optimize the workflow of 3DBP of cardiac tissues using a combination of tools from other disciplines that include structural mechanics-based microstructure modeling and advanced micro-CT-based image analysis. This study will also help develop new tools, technologies, and approaches for enhancing bioadditive manufacturing science overall.

2. MATERIALS AND METHODS

2.1. Hydrogel and Au-NPs. For making the 3DBP hydrogels, medium viscosity sodium alginate and gelatin from porcine skin were obtained from MP Biomedicals (Solon, OH, United States), which were the main components of the bioink mixture for bioprinting.[5] This bioink composition provides an ideal mixture for printing as well as provides biocompatibility based on published works.[6] 2 kDa methoxy-PEG coated gold nanoparticles (Au-NPs) with a core diameter of 60 nm and stock concentration of 2200 OD (optical density) were obtained from Luna Nanotech (Markham, ON, Canada) for the bioprinting as well.

2.2. Preparation and Characterization of Au-NP Solutions for 3DBP. The stock solution of 2 kDa methoxy-PEG coated Au-NPs was diluted 1:1000, 1:10 000, and 1:100 000 in molecular grade water to prepare solutions of varying concentrations (2.2, 0.22, and 0.022 OD respectively) for further characterization studies. UV−visible spectroscopy, dynamic light scattering (DLS), zeta potential measurement, and transmission electron microscopy (TEM) were used to characterize the Au-NP solutions.[7] Cell cytotoxicity studies were also performed to confirm the biocompatibility of the Au-NP solutions.

UV−visible spectroscopy from 400−850 nm was performed using the NanoDrop One Microvolume UV−vis Spectrophotometer (Thermo Fisher Scientific, Waltham, MA, United States). The maximum peak absorbance was used to calculate the concentration of the samples using Beer−Lambert Law.[8] The molar absorption

coefficient of the 60 nm Au-NPs was obtained from the product data sheet provided by the vendor. The hydrodynamic size,[9] polydispersity index (PDI),[9] and zeta potential[9] of the Au-NPs were measured using the Zetasizer Ultra Red (Malvern Panalytical, Malvern, UK). 1 mL of the Au-NP solutions in micro cuvettes was measured using the backscatter detection mode in order to obtain the hydrodynamic size and the PDI of the Au-NP solutions. Nanoparticle size and distribution are reported by intensity.[9] 1 mL of the gold nanoparticle solution was added into a folded capillary zeta cell to measure the zeta potential of Au-NPs.

TEM was performed on the Au-NP solutions to visualize the overall morphology and size distribution of the NPs as reported earlier.[10] The Au-NPs were air-dried on a plasma-treated TEM copper grid. Negative staining was performed with 0.2% uranyl acetate. Au-NPs were imaged using a JEOL 2010F 200 kV field emission analytical TEM with a Direct Electron DE-12 camera at the University of Oklahoma.[10]

For assessment of the in vitro biocompatibility of the Au-NPs, AC16 human cardiomyocyte cell lines (SCC109, EMD Millipore, MA) were cultured in Dulbecco's Modified Eagle's Medium/Nutrient Mixture (DMEM/F12, Sigma Cat. No. D6434, St. Louis, MO, United States), 10% FBS (EMD Millipore Cat. No. ES-009-B), and 1× penicillin−streptomycin solution (EMD Millipore Cat. No. TMS-AB2-C). One μL of the Au-NP solution studied was added into a six-well culture plate containing AC16 cells, with a density of approximately 60 000 cells per well and cultured for 2 days in an incubator under standard cell culture conditions. Cytotoxicity of the Au-NPs was measured using a Live−Dead Assay Kit (Thermo Fisher Scientific, USA) according to the protocol provided by the vendor. Calcein AM (green) stained live cells, while ethidium homodimer (red) was used to stain dead cells after being incubated in the samples for at least 1 h at room temperature (RT) (25 °C).[11] Live−dead assay images collected were analyzed by using ImageJ to determine cell viability. Live and dead cells were counted utilizing the cell-counter tool on ImageJ. % Cell viability (% live cells) versus % of dead cells was quantified using the following formula:

$$\text{no. of live/dead cells\%} = \frac{\text{number of live or dead cells}}{\text{total numbers of live + dead cells}} \times 100$$

2.3. Preparation of Alginate-Gelatin-Au-NP Hydrogels. To make the Au-NP alginate-gelatin-based hydrogels, 1 μL of the gold nanoparticle solution in the dilutions of 1:10 000 (high) and 1:100 000 (low) was added to 1000 μL of phosphate buffered saline (1X) (Cytiva, Marlborough, MA, United States), and the Au-NPs were mixed for a homogeneous distribution. Thereafter, 5% (w/v) gelatin and 7% (w/v) sodium alginate[6] were dissolved in the solution premixed with Au-NPs. Furthermore, for cellular scaffolds, half of the total volume of the resultant solution was composed of AC16 cardiomyocyte cell growth medium along with PBS (Section 2.5).

2.4. Three-Dimensional Bioprinting (3DBP). For making the 3DBP hydrogels, .STL files were designed using Fusion360 software v2.07421. The 3DBP acellular structures were printed by utilizing an accordion-like design (20 × 20 × 1 mm). An accordion-like design was used because it had been previously established as the ideal biofabrication geometry to recapitulate the native cardiac tissue anisotropic alignment found in vivo.[12] A Petri dish (100 mm diameter) was utilized as the printing base. Using a CELLINK BIO X 3D bioprinter (Blacksburg, VA), the structures were made utilizing the following parameters depicted in Table 1.

After the 3D structures were printed, they were cross-linked with 100 mM calcium chloride by pipetting 1000 μL of the solution into the Petri dish. The cross-linking solution was left in the Petri dish for 15 min, after which the solution was removed, and the 3D structures

Table 1. Printing Parameters

Nozzle Size	Printing Speed	Pressure	Temperature
22G	1 mm/s	45 kPa	25 °C

were rinsed thrice with 1× PBS. Following this step, they were used for further experimentation.

2.5. 3D Biocompatibility Studies with Au-NPs. 3D biocompatibility studies were performed by mixing AC16 cardiomyocytes into the bioink containing a solution of Au-NPs. To make the Au-NP alginate-gelatin-based hydrogels, 1 μL of the Au-NP solutions (1:10 000 and 1:100 000) was added to 1 mL of 1× PBS and well mixed. Thereafter, 5% (w/v) gelatin and 7% (w/v) sodium alginate were dissolved in the solution premixed with Au-NPs. Half of the total volume of the resultant solution (500 μL) was composed of AC16 cardiomyocyte cell growth medium along with 500 μL of PBS. The final cell density was 1×10^6 cells/mL in the bioink. Samples were maintained in culture for 48 h, after which the live−dead assay was performed. Cell viability was quantified using the formula reported above.

2.6. Scanning Electron Microscopy (SEM). SEM was used as a preliminary screening tool to study the acellular 3DBP Au-NP hydrogel structures for choosing the optimal concentrations of Au-NP solutions for embedding in the hydrogel for microcomputed tomography.

For doing this, two different Au-NP concentrations (1:10 000 (high) and 1:100 000 (low)) were used to print the acellular 3DBP scaffolds. SEM images were obtained by utilizing a Hitachi SU3500 Variable-Pressure Scanning Electron Microscope (Santa Clara, CA, United States). Optimization of the concentration of the Au-NPs in the 3DBP scaffolds that were further utilized for micro-CT was based on the SEM results obtained.

Obtained SEM micrographs were analyzed using their intensity profile in ImageJ using the following sequence under "analyze" > "histogram" > "intensity". From the obtained values, the mean intensity was calculated and reported as Mean + Standard deviation (AU).

2.7. Micro-CT for 3D Microstructure Visualization. Acellular 3D bioprinted scaffolds containing two different Au-NP concentrations (high and low) were bioprinted immediately before micro-CT imaging. In addition, 3DBP cellular scaffolds containing AC16 cardiomyocytes with either low or high concentrations of Au-NPs were also bioprinted immediately before micro-CT imaging. To prepare the samples for micro-CT imaging, samples with dimensions of 2 × 2 × 1 mm were isolated from all scaffolds, washed with 1× PBS three times, fixed with 4% PFA (15 min, RT) and scanned in distilled water at the University of Texas at Austin micro-CT Facility (Figure S1). The parameters used for the micro-CT scans are depicted in Table 2.

Table 2. Parameters Used for Micro-CT Scans

X-ray Settings	Value
Voltage (kV)	70
Power (W)	8.5
Filter	No filter
Acquisition Time (s)	0.05
Source-Object Distance (mm)	20.378
Detector-Object Distance (mm)	170.125

16 bit TIFF images were reconstructed by Xradia Reconstructor with a voxel size of 8.00 μm.[13] All images were obtained as slices from each sample, and each image slice was processed utilizing ImageJ software (NIH).[14] The processed images were used to create a z-stacked projection obtained by combining multiple image slices along the z-axis of the entire scaffold structure for both the acellular and the cellular samples. The z-stacked projections were used to extract maximum intensity images for all of the samples studied. These images represent the combination images of the slices with the highest intensity values, allowing for better visualization of the 3D scaffold structure. ImageJ software was further used to delineate the visible 3D scaffold structure as a region of interest (ROI) from the images obtained for both the acellular and the cellular samples. This step was necessary to enhance the visibility and quality of the scaffold structure.

The 3D volumetric reconstruction of the scaffold structure based on the micro-CT data and images was performed using Dragonfly software v.2022.2 (ORS, Montréal, Québec), which utilizes the obtained image data to reconstruct a 3D representation of the scaffolds. Dragonfly software was used for segmenting acellular and cellular scaffolds from micro-CT images. This process involved visualizing the structure of the scaffolds in 3D and extracting it using 2D region of interest (ROI) painter tools. The software has a feature called "multislice", which accelerated the process of ROI segmentation. Once the scaffolds were segmented, a 3D representation of the scaffold was generated, which was converted to a volumetric mesh to be used for further mechanical evaluation. This allowed for an in-depth analysis of the scaffold to gain valuable insights into the physical and mechanical properties of the 3DBP structure.

2.8. Rheological Analysis. In this study, both acellular and cellular 3DBP scaffolds were analyzed to evaluate their mechanical properties. For the cellular scaffolds, AC16 cells were mixed in the bioink to constitute a final cell seeding density of 9×10^5 cells/mL and printed to study the rheological properties of cell-based scaffolds in comparison with acellular controls. Rheometric analysis of the samples was conducted on an Anton-Paar MCR 92 rheometer (Anton-Paar, Austria) with a PP25/S measuring system and a 25 mm parallel plate with a 1 mm gap between the plate and the stage. From our previously published studies, the scaffold material's linear viscoelastic range (LVE) is known to be within a strain range of 0.1 to 150% at a constant frequency of 1 Hz.[6] From this evaluation, an optimal strain within the linear viscoelastic region was chosen to be kept constant during a frequency sweep from 100 to 0.1 rad/s. The mechanical properties of the cross-linked 3DBP acellular and cellular hydrogel scaffolds were evaluated 1 day post printing and after swelling in PBS (pH 7.4) or in cell-culture media, respectively. Storage/loss moduli, complex viscosity, and elastic modulus were measured at 1.99 Hz and reported to analyze the mechanical stability of the scaffolds.[6]

2.9. Structural Analysis. Tetrahedral meshing was adopted to evaluate the mechanical properties of acellular and cellular scaffolds using ANSYS (Version: 2021 R2, Canonsburg, PA), which is a crucial step in the finite element analysis (FEA) process. This involved dividing the geometry (.stl file) into small elements to approximate the continuous structure, allowing for the analysis of the complex geometry and for obtaining accurate and reliable results. Given the complex geometry of our structures and their resulting microstructures, an efficient way of simulating their mechanical parameters via loading was to homogenize their material properties. For this purpose, an Ansys Material Designer with the hybrid meshing feature was adopted to optimize microstructures and homogenize the material properties of complex composite scaffolds containing cells and Au-NPs. To refine the mesh in certain regions of interest, such as in areas of high stress gradients, the number of nodes reported was 144 485, and the number of elements was 25 965. For running the simulations by applying a load of 9.3 N[15] along the geometry's front face while fixing the back face, the following parameters were adopted for acellular and cellular scaffolds, as depicted in Table 3. A Poisson's ratio of 0.5 was assumed for hydrogels and polymers.[16] The density, thermal conductivity, tensile yield, and ultimate strength were all assumed based on values in existing literature reports.[17−19]

Table 3. Parameters for ANSYS Simulation

Parameters	Acellular	Cellular
Young's Modulus (Pa)	44 918.61	18 487.02
Bulk Modulus (Pa)	7.4864e+05	3.0812e+05
Shear Modulus (Pa)	15 073	6203.7
Force (N)	9.3	
Density (g/mL)	1.053	
Thermal Conductivity (W/mK)	0.06−0.30	
Tensile Yield Strength (kPa)	70	
Tensile Ultimate Strength (kPa)	40	
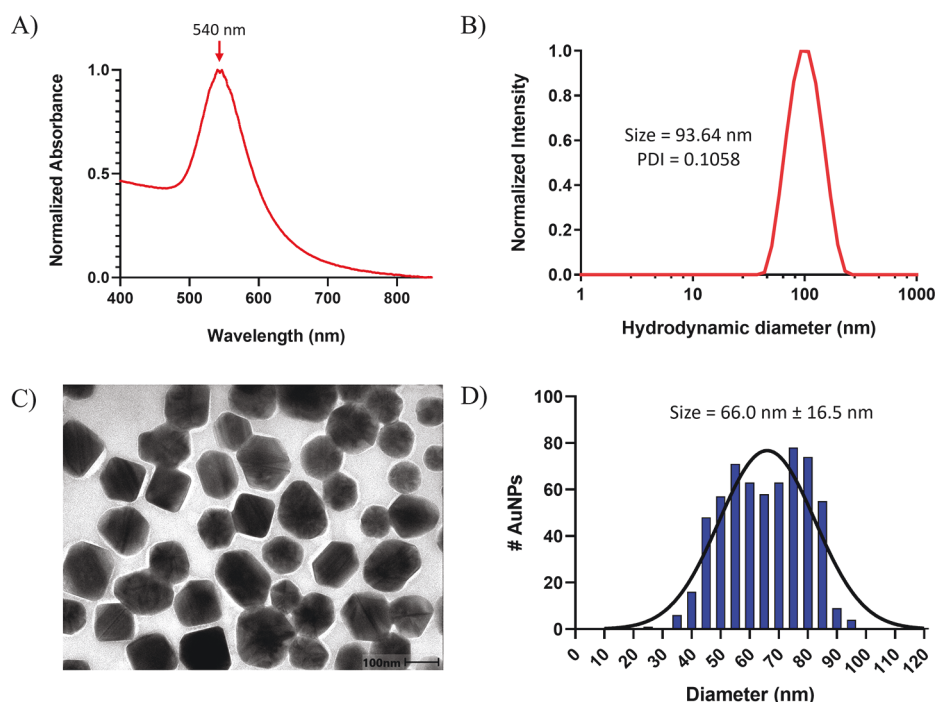
Figure 1. (A) Normalized absorbance spectra of Au-NPs as determined by UV−vis spectroscopy. (B) Hydrodynamic diameter of Au-NPs as determined by DLS. (C) Representative TEM micrograph of 2 kDa methoxy-PEG coated Au-NPs; scale bar is 100 nm. (D) Histogram and Gaussian fits of the measured Au-NP size distribution as determined from TEM micrographs (n = 6000 nanoparticles).

The mechanical properties of the scaffolds were examined using a static structural model in ANSYS. The resultant elastic stress, strain, and total deformation were evaluated and compared between acellular and cellular scaffolds as well as with results obtained from rheological analysis and micro-CT scanning.

2.10. Statistical Analysis. All samples were analyzed in triplicate, unless otherwise specified. Data are represented as the mean ± standard deviation. Comparison of the means of two independent samples was performed by t test (GraphPad Prism 9) to determine if the averages of any two of the sample data sets compared showed a significant difference in their values. $P < 0.05$ was considered statistically significant. The data sets generated during and/or analyzed during the current study are available from the corresponding author upon reasonable request.

3. RESULTS

3.1. Au-NP Solution Preparation, Characterization, and Cytotoxicity Analysis. We first prepared and characterized the 2 kDa methoxy-PEG coated 60 nm Au-NP solutions that were to be incorporated into the 3D-printed alginate-gelatin-based hydrogels. Au-NPs were characterized by using UV−visible spectrometry, dynamic light scattering (DLS), zeta potential measurement, and transmission electron microscopy (TEM). The characterization data are presented in Figure 1. The absorbance spectra as determined by UV−visible spectroscopy showed the expected characteristic absorbance peak at between 540 and 548 nm for 60−70 nm Au-NPs (Figure 1A).[9] DLS determined that the hydrodynamic diameter of Au-NPs was 93.64 nm, with a PDI of 0.1058 (Figure 1B).[9] The zeta potential of the Au-NPs was measured to be −37.5 mV, indicating colloidal stability.[10] A representative TEM micrograph of Au-NPs is shown in Figure 1C. Analysis of TEM images showed that the Au-NPs were spherical in shape with a mean core diameter of 66 ±16.5 nm (Figure 1D).[10]

Figure 2 represents the live−dead florescent microscopy images (Figure 2A) of AC16 cells treated with 1:10 000 Au-
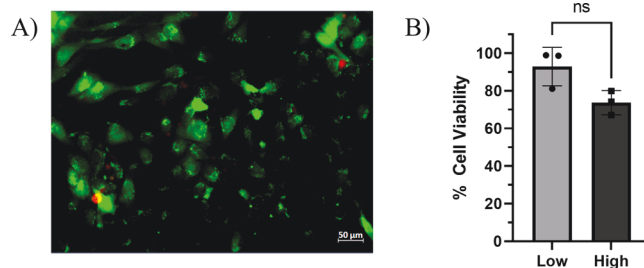
Figure 2. Cell viability in 1:10 000 (high concentration) Au-NP and in 1:100 000 (low concentration) Au-NP solutions. (A) Live cells stained green by calcein AM and dead cells stained red by ethidium homodimer after 2 days in culture. (B) Viability percentage in 2D cell culture for both 1:10 000 and 1:100 000 Au-NP samples after 2 days in culture.

NPs and 1:100 000 Au-NPs respectively in 2D culture conditions. Live cells are stained green, whereas dead cells are stained red. The percentage of cell viability is shown in Figure 2B and was calculated using the equation described in section 2.2. In samples containing 1:10 000 Au-NPs and 1:100 000 Au-NPs, the percentage of viability was found to be equal to 74 ± 6.4% and 93 ± 10% respectively. From these results, we concluded that the Au-NP solutions in a 1:10 000 ratio were not cytotoxic; however, the 1:100 000 concentration was partially cytotoxic.

3.2. Scanning Electron Microscopy (SEM). Figure 3A shows the SEM micrographs obtained for control samples (without Au-NPs) to observe the baseline resolution, contrast, and optimum image quality of the scaffolds. Figures 3B,C depict images obtained from samples containing low and high
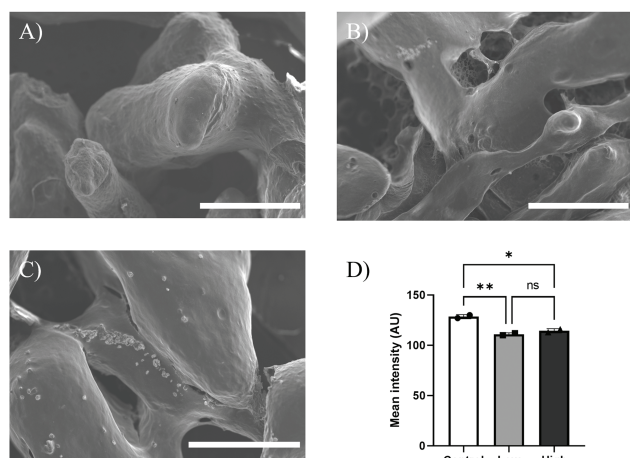
Figure 3. SEM images obtained for samples (A) without Au-NPs, (B) with a low concentration (1:100,000 dilution) of Au-NPs, and (C) with a high concentration (1:10 000 dilution) of Au-NPs. All scale bars represent 1 mm in length. Shown in (D) is a graph with mean intensity profiles of all samples ($n = 2$). * represents $p < 0.05$, ** represents $p < 0.01$, and ns represents statistically not significant.

concentrations of Au-NPs, respectively. Figure 3D shows a quantitative comparison of the mean intensity profile of the images obtained for samples containing varying amounts of Au-NPs. The results revealed statistically significant differences in image contrast and intensity, enabling us to differentiate between samples made without and with varying concentrations of Au-NP solutions. The samples containing high concentrations of Au-NPs showed visible nanoparticle aggregates on SEM micrographs and reduced the mean intensity of the sample struts analyzed by using ImageJ.

3.3. 3D Biocompatibility of Au-NPs. Figure 4 represents the live−dead florescent microscopy images (Figure 4A) of
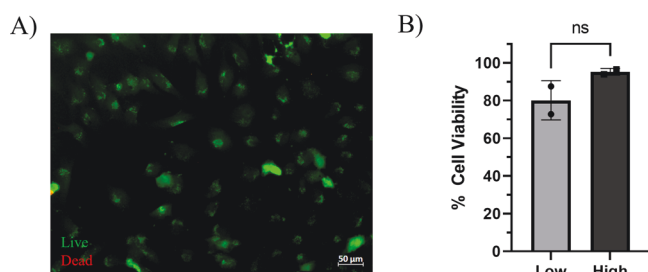

Figure 4. Cell viability in 3D samples containing varying concentrations of Au-NPs and cells. (A) Live cells stained green by calcein AM and dead cells stained red by ethidium homodimer. (B) Viability percentage in 3D cell cultures ($n = 2$).

AC16 cells 3D bioprinted within gels containing high and low concentrations of Au-NPs. In samples containing a high concentration of Au-NPs, the percentage of cell viability was found to be equal to $95 \pm 1.8\%$ in comparison with the low concentration, which depicted cell viability to be $80 \pm 10\%$. From these results, we concluded that the Au-NPs were not cytotoxic to cells when they were in close contact in the 3D bioprinted gels.

3.4. Microcomputed Tomography (micro-CT) and 3D Structure Visualization. The samples containing 1:100 000 (low concentration) Au-NPs could not be imaged using micro-

CT as clearly as the scaffolds without any Au-NPs. Conversely, we were able to obtain 595 micro-CT image slices from acellular scaffolds containing 1:10 000 (high concentration) Au-NPs. Similarly, 657 sliced images were obtained from scaffolds containing 1:10 000 (high concentration) Au-NPs with AC16 cells. Both sets of micro-CT images obtained were processed using ImageJ software to create a z-stacked projection. The stacked 3D projections obtained for both samples (acellular and cellular) were processed to obtain the maximum intensity images, as shown in Figure 5. The entire
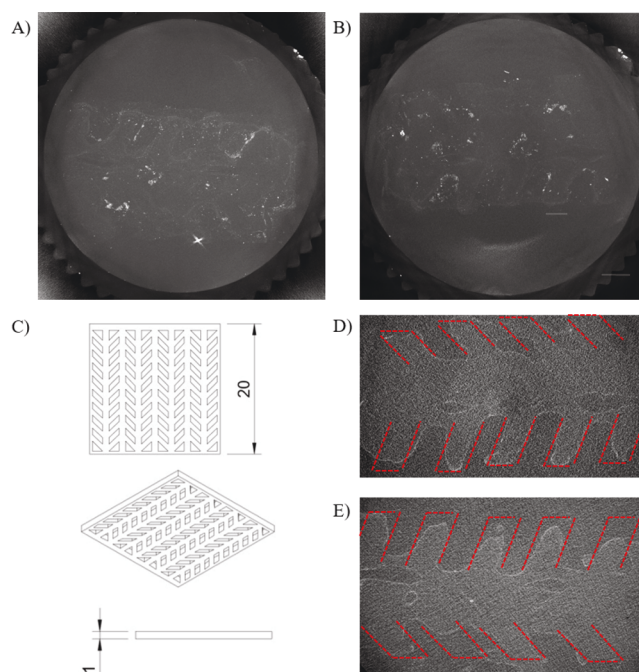
Figure 5. Microcomputed tomography results for (A) acellular sample containing 1:10 000 (high concentration) Au-NPs and (B) sample containing 1:10 000 (high concentration) of Au-NPs and AC16 cardiomyocytes. Shown are 3D z-stacked images of the samples studied. (C) 3D STL design ($20 \times 20 \times 1$ mm) utilized for the 3D bioprinting process of scaffolds. (D) Microcomputed tomography results for acellular scaffold containing 1:10 000 (high concentration) Au-NPs and (E) scaffold containing 1:10 000 (high concentration) of Au-NPs and AC16 cardiomyocytes.

3D scaffold structure can be observed in Figure 5A for the acellular sample and Figure 5B for the scaffold containing AC16 cells, both samples containing 1:10 000 (high concentration) Au-NPs. These images were processed using ImageJ to extract the visible scaffold structure. Furthermore, Figure 5C shows the 3D .STL design used for this study. Figure 5D shows an image outline obtained for the acellular scaffold, and Figure 5E is an image outline of the scaffold containing AC16 cardiomyocytes. As can be observed in these figures, addition of the Au-NPs enhanced the resolution and quality of the images, which allowed for the visualization of the micro-structure of the 3D bioprinted scaffolds using micro-CT. As well, the micro-CT images as annotated with red dotted lines in Figure 5D,E, obtained for both samples, resembled the design utilized to fabricate these scaffolds as expected.

From this information, the 3D reconstruction of the structure was performed using Dragonfly software, and results obtained from this reconstruction are observed in Figure 6. Figure S2 depicts the overview of the ROI segmentation
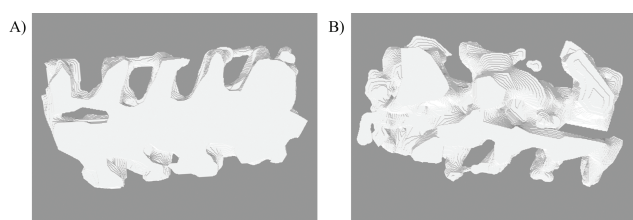
Figure 6. (A) 3D reconstruction of acellular scaffold. (B) 3D reconstruction of cellular scaffold.

process that was carried out using Dragonfly software. In Figure S2A, an initial 3D visualization of the acellular scaffold is shown, which was created by manipulating the image's window labeling (Supporting Information Video 1: 3D Structure Visualization.avi). This was done in order to remove any overlap between the air/water and scaffold intensities. Figure S2B shows the 3D structure that was segmented and highlighted in green in both the 3D view and orthogonal views (XY, XZ, and YZ). Figure 6 presents the final 3D reconstruction of both acellular and cellular scaffolds. As can be observed from Figure 6A, the acellular scaffold depicts more structural complexity as well as a more-intact structure. On the other hand, Figure 6B shows the cellular scaffold, which revealed structural dissolution owing to biodegradation due to the presence of the cells remodeling the scaffold, thereby affecting the quality and resolution of the 3D reconstruction for this sample. Our results showed a higher definition of the overall structure of the 3DBP scaffolds due to the inclusion of the Au-NPs.

This study also evaluated the effect of encapsulating Au-NPs and cells on the mechanical properties of the hydrogels postprinting and 24 h after in vitro incubation. Analysis was conducted on samples evaluated within the LVE range under constant shear strain. Results presented in Figure 7A depict a significantly higher storage/loss modulus in the acellular scaffolds containing the Au-NPs (14.9 ± 0.8/1.43 ± 0.19 KPa; $p < 0.05$) as compared to those in cellular scaffolds (6.15 ± 0.19/0.32 ± 0.08 KPa; $p < 0.05$). Likewise, both the complex viscosity (Figure 7B) (2 383 100 ± 129 400.54/980 820 ± 28 963.09 mPa·S; $p < 0.05$) and elastic moduli (Figure 7C) (44.92 ± 2.46/18.49 ± 0.61 KPa; $p < 0.05$) appeared to be greater in the acellular scaffolds with Au-NPs with respect to those in cellular scaffolds. These results confirmed that the addition of Au-NPs enhanced the overall mechanical properties of the 3DBP scaffolds as indicated by our previously published works.[20] However, the inclusion of cells led to the biodegradation of the scaffolds during in vitro incubation, as shown by the reduction in the values of storage/loss modulus in cellular scaffolds. Similarly, both the complex viscosity and the elastic moduli were higher in magnitude in the acellular scaffolds containing Au-NPs compared with those in the cellular scaffolds. These mechanical parameters were further adopted for the mechanical analysis of the scaffolds. Comparison between the acellular and cellular scaffolds yielded the following results as shown in Table 4a,b, when applied with equivalent stress of a minimum of 8.79 Pa, a maximum of 712.88 Pa, with an average of 234.22 Pa for both acellular and cellular scaffolds.

Table 4. Total Deformation, Elastic Strain, and Stress

	a. Total Deformation (m)		
	Minimum (m)	Maximum (m)	Average (m)
Acellular	0	5.9394e−005	1.3292e−005
Cellular	0	1.4431e−004	3.2295e−005
	b. Equivalent Elastic strain (m/m)		
	Minimum (m/m)	Maximum (m/m)	Average (m/m)
Acellular	2.0667e−004	1.587e−002	5.4815e−003
Cellular	5.0215e−004	3.8561e−002	1.3319e−002

Within a 24 h incubation period, mechanical properties of cellular scaffolds significantly increased in comparison to acellular scaffolds due to the rearrangement and remodeling of cells within the 3D structure, which provided them with a favorable framework to grow.[21] Additionally, the AC16 cardiomyocytes can double in number in around 24 h, which contributes to enhanced mechanical properties post in vitro incubation.

Our results demonstrated that the resultant elastic strain and total deformation were greater in the cellular scaffolds compared with those in the acellular scaffolds. These findings corroborate with the rheological analysis data, as the acellular scaffolds yielded a higher elastic and storage moduli and therefore resisted deformation and elongation. On the contrary, the cellular scaffolds retained more water because of the increased cellular content and depicted lower elastic and storage moduli. This enabled them to exhibit enhanced degrees of strain and deformation. Furthermore, the inclusion of cells enabled the scaffolds to be remodeled, as revealed by the micro-CT results, which also enabled the structure to biodegrade and resulted in more strain and deformation. Figure S3 depicts the results of the mechanical simulation of a scaffold containing cells and Au-NPs.
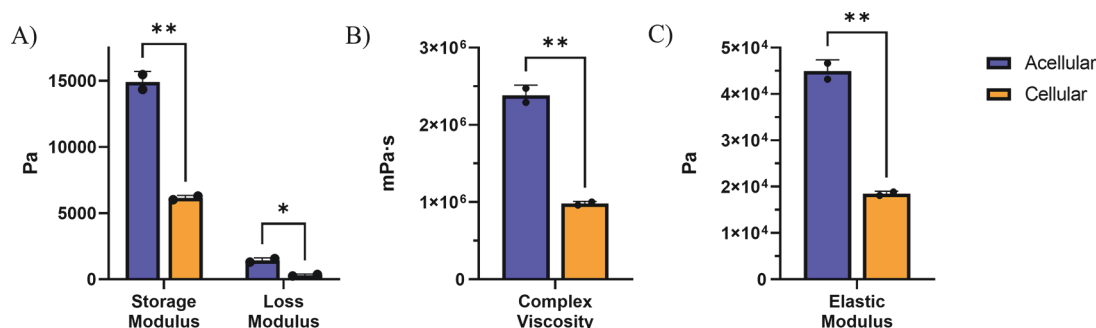
Figure 7. (A) Storage and loss modulus for the acellular and cellular scaffolds. (B) Complex viscosity for the acellular and cellular scaffolds. (C) Calculated elastic modulus for the acellular and cellular scaffolds ($n = 2$), where * represents $p < 0.05$, and ** represents $p < 0.01$.

4. DISCUSSION

It is important to reiterate the role of scaffolds in tissue engineering as substrates that can mimic the native ECM, which are known to control and influence cell attachment, proliferation, and differentiation.[22] The response of a scaffold is significantly influenced by the properties and composition of its constituents or its microstructure. Additionally, for biomaterial scaffolds, the microstructure poses as a mechanical cue, which can influence cell behaviors and control key functions at the molecular and cellular levels. Microstructure plays an essential role in the control of 3D bioprinted scaffold's mechanical properties, and variable microstructures can be produced by altering the gel parameters.[23] The effect of the chemical cross-linking (gelling) parameters on the viscoelastic and diffusion properties of the scaffolds as well as other structural parameters (e.g., pore size, extent of porosity, average molecular weight of the polymer chain between neighboring cross-links, cross-linking density) can all affect the resultant microstructure and overall mechanical properties. This aspect of dynamic microstructure modulation, which can affect cell fate and turnover, has been mostly overlooked by the 3D bioprinting community. Thus, it is important to understand the process of layer-by-layer 3D printing followed by chemical cross-linking and the relationship of component, structure, property, and application of the printed biological constructs from a microstructure perspective.[24] Additive manufacturing can generate anisotropic bulk material properties from an isotropic build material.[25] Since precise and reliable prediction of macroscale material properties from the microscale components is an active and emerging area of research; optimization of the microstructure with the goal of obtaining a resultant tissue structure that is functionally robust is critical.

The objective of this study was to adopt the micro-CT technique for imaging of 3DBP scaffolds embedded with a Au-NP microstructure evaluation. Micro-CT is a nondestructive imaging method that utilizes X-rays to rapidly digitize samples in three dimensions.[26] The ongoing advancements in this field have resulted in the development of X-ray micro-CT scanners with submicron resolution.[13] Although dense structures such as bones can be visualized without any specific preparation,[27] a limitation of micro-CT scanners is the low contrast of soft tissues due to low X-ray absorption, which can be overcome using contrast agents.[28] The inclusion of an appropriate contrast agent such as Au-NPs presents a nondestructive evaluation approach, which has the potential to enhance the biomanufacturing workflow of these tissue engineered structures for clinical applications without the need to stain them as stains can alter the characteristics of the tissues, and their removal is challenging.[29] This will also help understand how the environmental and biodegradation leads to alteration in the microstructure, leading to variations in the biomechanical properties for 3D-printed scaffolds.

Although prior studies have adopted micro-CT-based imaging to visualize individual cells within thin collagen gels in the absence of any exogenous contrast, the image resolution and contrast from these studies are extremely poor.[30] Others have been shown to adopt X-ray-based imaging toward the characterization of biomaterial scaffolds used for tissue engineering. These experiments demonstrate the ability of X-ray CT to provide sufficient contrast for identification of individual cells within a biomaterial environment and the fact that this information can be used to provide quantitative

information about cell placement within scaffolds. Such reports motivated us to adopt micro-CT-based imaging to study and analyzed our 3DBP scaffolds.[30−32]

The inclusion of Au-NPs in alginate-gelatin 3DBP scaffolds was done and studied for the first time in the field of tissue engineering by our group. Prior to this, our group[33] and others[34] have developed NP-embedded hydrogels for other applications, which provide the knowledge base and premise for this study. The main benefit of using micro-CT imaging is the generation of a series of projection images (radiographs) that can be reconstructed into cross-sectional images using reconstruction algorithms as detailed in the image acquisition workflow. However, the 3D reconstructed images that are used to recreate the scaffold as a 3D object can only be of a limited size range and can deliver insights into scaffold remodeling and degradation over a limited scale. Briefly, micro-CT was performed on an approximately 2×2 mm small cut-section of the 3DBP structure. In this particular scenario, only qualitative results were extracted from the X-ray and reconstructed image of the hydrogel.[35] For instance, these results allowed for the visual detection of physical degradation of the cellular sample. For further studies, we intend to scan the full 20×20 mm 3DBP accordion structure and have both qualitative and quantitative results for visualization and analysis. Such results can aid on the comparison across samples and reveal different structural and morphological properties relevant to this study like pore distribution, pore size, surface area per unit volume, and more.[36] This technique demonstrates the feasibility of utilizing micro-CT in characterizing the 3D bioprinted constructs.

Furthermore, 3D geometric morphometric methods via mechanical modeling and simulation have to be applied in addition to for comparisons between different results through the creation of surface models and the application of specified landmarks on them.

From the contrast enhancement using gold nanoparticles perspective, colloidal stability and dispersion of the Au-NPs in the 3D bioprinted scaffolds are important in order to provide uniform contrast throughout the structure during micro-CT imaging. We initially tested citrate-coated gold nanoparticles in this 3D bioprinted system but were unable to obtain workable micro-CT images due to the extensive aggregation of gold nanoparticles (data not shown). We hypothesize this is due to the extensive salt concentration used in the 3D bioprinting matrix and cross-linking solution. PEGylation of nanoparticles is a well-established method to increase the colloidal stability and dispersion of nanoparticles due to increase in steric hindrance of the nanosystem.[37]

We expected samples with Au-NPs to depict enhanced contrast, resolution, and quality in a dose-dependent manner in comparison to samples without Au-NPs. Furthermore, if the SEM image from a particular sample set depicted enhanced contrast and resolution, we expected that particular dose of Au-NPs to reveal the similar enhancement in image quality when analyzed using micro-CT. In our SEM images, we can still observe minor aggregations of PEGylated gold nanoparticles, although this did not seem to significantly alter the micro-CT imaging quality. The dispersion of gold nanoparticles in the 3D bioprinting matrix is essentially random, since the nanoparticles are simply mixed into the matrix before bioprinting. The diffusion of gold nanoparticles is severely limited due to the high viscosity of the 3D bioprinted material, but they may become concentrated locally by the 3D printing process[38] or

relocated in the biomaterial postprinting by the embedded cells.[39] Some strategies to increase, better control, and maintain the uniform dispersion of gold nanoparticles throughout the 3D bioprinted material include the addition of chemical moieties on the gold nanoparticle surface to anchor them covalently to the biomatrix[39] and further advancements in implementing the 3D bioprinting process for selective deposition and preferential alignment of nanoparticles.[38] The size of the gold nanoparticle and concentration are also very important in controlling the amount of micro-CT contrast. Micro-CT contrast increases proportionally to both nanoparticle size and concentration.[40] There is a trade-off between using larger-sized gold nanoparticles versus using higher concentrations of smaller-sized gold nanoparticles for more micro-CT imaging contrast. Larger size gold nanoparticles are more likely to disrupt the native microstructure of the bioprinted scaffold due to modified mechanical properties of the nanoparticle-laden composite biomaterial and being similarly sized to the micronozzle in the 3D printer,[34,41,42] but theoretically, a lower concentration can be used to achieve high and sufficient micro-CT imaging contrast. On the other hand, smaller size gold nanoparticles are less likely to disrupt the native microstructure of the bioprinted scaffolds, but higher concentrations need to be used, and this may cause cellular toxicity or disrupt the cellular homeostasis in the codeposited cells.[43]

Future work for this project will include the optimization of different concentrations of gold nanoparticles to compare the image resolution, quality, and visibility of the microstructure of hydrogels. Additionally, the calculation of the mechanical properties of the 3D bioprinted scaffold from the micro-CT data obtained will be performed as the next step for this project.

5. CONCLUSION

In conclusion, this study successfully prepared and characterized methoxy-PEG coated Au-NP solutions for incorporation into 3D-printed alginate-gelatin hydrogels. The characterization results confirmed the physicochemical properties of the Au-NPs. Cytotoxicity analysis demonstrated the nontoxic nature of the Au-NP solutions, as evidenced by high cell viability percentages in both 2D and 3D culture conditions. SEM analysis revealed distinguishable differences in image contrast and intensity between samples with and without Au-NPs, with high concentrations of Au-NPs displaying visible nanoparticle aggregates. Micro-CT imaging demonstrated that the addition of Au-NPs enhanced the resolution and quality of the images, allowing for visualization of the microstructure of the 3D bioprinted scaffolds. The application of gold nanoparticles as contrast agents did have a significant impact on the resolution and quality of images obtained from micro-CT. Furthermore, 3D reconstruction of the scaffold structures confirmed the improved visualization and showed that the presence of Au-NPs increased the overall structural complexity. Additionally, mechanical analysis revealed that the inclusion of Au-NPs enhanced the mechanical properties of acellular scaffolds, but the presence of cells led to biodegradation and reduced mechanical strength. These findings highlight the potential of Au-NPs to enhance the properties and imaging capabilities of 3D-printed hydrogels for tissue engineering applications. Further research can focus on optimizing the concentration and distribution of Au-NPs to maximize the desired effects while minimizing biodegradation in cellular scaffolds.

■ ASSOCIATED CONTENT

Ⓢ Supporting Information

The Supporting Information is available free of charge at https://pubs.acs.org/doi/10.1021/acsabm.3c00621.

Figure S1 - microCT imaging setup; Figure S2 - overall process of 3D segmentation and meshing of scaffolds; Figure S3 - structural meshing to evaluate mechanical properties of 3D bioprinted scaffolds (PDF)

Video S1 - 3D structure visualization of the reconstructed structure from micro-CT (MP4)

■ AUTHOR INFORMATION

Corresponding Authors

Wilson Poon − *Department of Metallurgical, Materials, and Biomedical Engineering and Delivery Systems and Nano-Therapeutics Innovation Laboratory (DESTINATION), The University of Texas at El Paso, El Paso, Texas 79968, United States;* ⓞ orcid.org/0000-0003-2192-3077; Email: wpoon@utep.edu

Binata Joddar − *Inspired Materials & Stem-Cell Based Tissue Engineering Laboratory (IMSTEL), The University of Texas at El Paso, El Paso, Texas 79968, United States; Department of Metallurgical, Materials, and Biomedical Engineering, The University of Texas at El Paso, El Paso, Texas 79968, United States; Border Biomedical Research Center, The University of Texas at El Paso, El Paso, Texas 79968, United States;* ⓞ orcid.org/0000-0002-9157-3140; Email: bjoddar@utep.edu

Authors

Salma P. Ramirez − *Inspired Materials & Stem-Cell Based Tissue Engineering Laboratory (IMSTEL), The University of Texas at El Paso, El Paso, Texas 79968, United States; Department of Metallurgical, Materials, and Biomedical Engineering, The University of Texas at El Paso, El Paso, Texas 79968, United States*

Ivana Hernandez − *Inspired Materials & Stem-Cell Based Tissue Engineering Laboratory (IMSTEL), The University of Texas at El Paso, El Paso, Texas 79968, United States; Department of Metallurgical, Materials, and Biomedical Engineering, The University of Texas at El Paso, El Paso, Texas 79968, United States*

Hannia V. Balcorta − *Department of Metallurgical, Materials, and Biomedical Engineering and Delivery Systems and Nano-Therapeutics Innovation Laboratory (DESTINATION), The University of Texas at El Paso, El Paso, Texas 79968, United States*

Piyush Kumar − *Department of Aerospace and Mechanical Engineering, The University of Texas at El Paso, El Paso, Texas 79968, United States*

Vinod Kumar − *Department of Aerospace and Mechanical Engineering, The University of Texas at El Paso, El Paso, Texas 79968, United States*

Complete contact information is available at:
https://pubs.acs.org/10.1021/acsabm.3c00621

Author Contributions

S.P.R. and I.H. have equal contribution as first coauthors.

■ REFERENCES

(1) Khademhosseini, A.; Langer, R. A decade of progress in tissue engineering. *Nature protocols* **2016**, *11* (10), 1775−1781.

(2) Ikada, Y. Challenges in tissue engineering. *J. R. Soc., Interface* **2006**, *3* (10), 589−601.

(3) Chen, P. Y.; Lin, A. Y. M.; Lin, Y. S.; Seki, Y.; Stokes, A. G.; Peyras, J.; Olevsky, E. A.; Meyers, M. A.; McKittrick, J. Structure and mechanical properties of selected biological materials. *Journal of the mechanical behavior of biomedical materials* **2008**, *1* (3), 208−226.

(4) Wu, Y.; Ali, M. R.; Chen, K.; Fang, N.; El-Sayed, M. A. Gold nanoparticles in biological optical imaging. *Nano Today* **2019**, *24*, 120−140.

(5) Joddar, B.; Tasnim, N.; Thakur, V.; Kumar, A.; McCallum, R. W.; Chattopadhyay, M. Delivery of mesenchymal stem cells from gelatin-alginate hydrogels to stomach lumen for treatment of gastroparesis. *Bioengineering* **2018**, *5* (1), 12.

(6) Alonzo, M.; El Khoury, R.; Nagiah, N.; Thakur, V.; Chattopadhyay, M.; Joddar, B. 3D Biofabrication of a Cardiac Tissue Construct for Sustained Longevity and Function. *ACS Appl. Mater. Interfaces* **2022**, *14* (19), 21800−21813.

(7) Sobczak-Kupiec, A.; Malina, D.; Zimowska, M.; Wzorek, Z. Characterization of gold nanoparticles for various medical application. *Dig J. Nanomater Bios* **2011**, *6* (2), 803−808.

(8) Chithrani, B. D.; Ghazani, A. A.; Chan, W. C. W. Determining the Size and Shape Dependence of Gold Nanoparticle Uptake into Mammalian Cells. *Nano Lett.* **2006**, *6* (4), 662−668.

(9) Perrault, S. D.; Chan, W. C. W. Synthesis and Surface Modification of Highly Monodispersed, Spherical Gold Nanoparticles of 50−200 nm. *J. Am. Chem. Soc.* **2009**, *131* (47), 17042−17043.

(10) Frickenstein, A. N.; Mukherjee, S.; Harcourt, T.; He, Y.; Sheth, V.; Wang, L.; Malik, Z.; Wilhelm, S. Quantification of monodisperse and biocompatible gold nanoparticles by single-particle ICP-MS. *Anal. Bioanal. Chem.* **2023**, *415* (18), 4353−4366.

(11) El Khoury, R.; Ramirez, S. P.; Loyola, C. D.; Joddar, B. Demonstration of doxorubicin's cardiotoxicity and screening using a 3D bioprinted spheroidal droplet-based system. *RSC Adv.* **2023**, *13* (12), 8338−8351.

(12) Engelmayr, G. C., Jr.; Cheng, M.; Bettinger, C. J.; Borenstein, J. T.; Langer, R.; Freed, L. E. Accordion-like honeycombs for tissue engineering of cardiac anisotropy. *Nat. Mater.* **2008**, *7* (12), 1003−10.

(13) Hanna, R. D.; Ketcham, R. A. Evidence for accretion of fine-grained rims in a turbulent nebula for CM Murchison. *Earth and Planetary Science Letters* **2018**, *481*, 201−211.

(14) Collins, T. J. ImageJ for microscopy. *Biotechniques* **2007**, *43* (S1), S25−S30.

(15) Hartrumpf, M.; Sterner, J.; Schroeter, F.; Kuehnel, R. U.; Ostovar, R.; Albes, J. M. How Strong Can We Pull? Critical Thresholds for Traction Forces on the Aortic Annulus: Measurements on Fresh Porcine Hearts. *Medicina* **2022**, *58* (8), 1055.

(16) Javanmardi, Y.; Colin-York, H.; Szita, N.; Fritzsche, M.; Moeendarbary, E. Quantifying cell-generated forces: Poisson's ratio matters. *Communications Physics* **2021**, *4* (1), 237.

(17) Vinnakota, K. C.; Bassingthwaighte, J. B. Myocardial density and composition: a basis for calculating intracellular metabolite concentrations. *American Journal of Physiology-Heart and Circulatory Physiology* **2004**, *286* (5), H1742−H1749.

(18) De la Cruz, L. G.; Abt, T.; León, N.; Wang, L.; Sánchez-Soto, M. Ice-Template Crosslinked PVA Aerogels Modified with Tannic Acid and Sodium Alginate. *Gels* **2022**, *8* (7), 419.

(19) Drury, J. L.; Dennis, R. G.; Mooney, D. J. The tensile properties of alginate hydrogels. *Biomaterials* **2004**, *25* (16), 3187−3199.

(20) Alvarez-Primo, F.; Anil Kumar, S.; Manciu, F. S.; Joddar, B. Fabrication of surfactant-dispersed HiPco single-walled carbon nanotube-based alginate hydrogel composites as cellular products. *International Journal of Molecular Sciences* **2019**, *20* (19), 4802.

(21) Davidson, M. M.; Nesti, C.; Palenzuela, L.; Walker, W. F.; Hernandez, E.; Protas, L.; Hirano, M.; Isaac, N. D. Novel cell lines derived from adult human ventricular cardiomyocytes. *Journal of molecular and cellular cardiology* **2005**, *39* (1), 133−147.

(22) Chung, S.; King, M. W. Design concepts and strategies for tissue engineering scaffolds. *Biotechnology and applied biochemistry* **2011**, *58* (6), 423−438.

(23) Karvinen, J.; Ihalainen, T. O.; Calejo, M. T.; Jönkkäri, I.; Kellomäki, M. Characterization of the microstructure of hydrazone crosslinked polysaccharide-based hydrogels through rheological and diffusion studies. *Materials Science and Engineering: C* **2019**, *94*, 1056−1066.

(24) Li, S.; Jiang, Z.; Han, J.; Xu, Z.; Wang, C.; Huang, H.; Yu, C.; Lee, S.-J.; Pianetta, P.; Ohldag, H.; Qiu, J.; Lee, J.-S.; Lin, F.; Zhao, K.; Liu, Y. Mutual modulation between surface chemistry and bulk microstructure within secondary particles of nickel-rich layered oxides. *Nat. Commun.* **2020**, *11* (1), 4433.

(25) Wang, Z.; Palmer, T. A.; Beese, A. M. Effect of processing parameters on microstructure and tensile properties of austenitic stainless steel 304L made by directed energy deposition additive manufacturing. *Acta Mater.* **2016**, *110*, 226−235.

(26) Keklikoglou, K.; Arvanitidis, C.; Chatzigeorgiou, G.; Chatzinikolaou, E.; Karagiannidis, E.; Koletsa, T.; Magoulas, A.; Makris, K.; Mavrothalassitis, G.; Papanagnou, E. D.; Papazoglou, A. S.; Pavloudi, C.; Trougakos, I. P.; Vasileiadou, K.; Vogiatzi, A. Micro-CT for Biological and Biomedical Studies: A Comparison of Imaging Techniques. *J. Imaging* **2021**, *7* (9), 172.

(27) Bilecenoğlu, B.; Ocak, M. Analysis of Fracture Callus Mechanical Properties Using Micro-CT. *Micro-computed Tomography (micro-CT) in Medicine and Engineering* **2020**, 77−85.

(28) Keklikoglou, K.; Faulwetter, S.; Chatzinikolaou, E.; Wils, P.; Brecko, J.; Kvaček, J.; Metscher, B.; Arvanitidis, C. Micro-computed tomography for natural history specimens: a handbook of best practice protocols. *European Journal of Taxonomy* **2019**, No. 522, 1−55.

(29) Schmidbaur, H.; Keklikoglou, K.; Metscher, B. D.; Faulwetter, S. Exploring methods to remove iodine and phosphotungstic acid stains from zoological specimens. *Bruker microCT User Meeting* **2015**, *21*, 1−8.

(30) Appel, A.; Anastasio, M. A.; Brey, E. M. Potential for imaging engineered tissues with X-ray phase contrast. *Tissue Engineering Part B: Reviews* **2011**, *17* (5), 321−330.

(31) Li, L.; Gil, C. J.; Finamore, T. A.; Evans, C. J.; Tomov, M. L.; Ning, L.; Theus, A.; Kabboul, G.; Serpooshan, V.; Roeder, R. K. Methacrylate-modified gold nanoparticles enable noninvasive monitoring of photocrosslinked hydrogel scaffolds. *Advanced NanoBiomed Research* **2022**, *2* (7), 2200022.

(32) Celikkin, N.; Mastrogiacomo, S.; Walboomers, X. F.; Swieszkowski, W. Enhancing X-ray attenuation of 3D printed gelatin methacrylate (GelMA) hydrogels utilizing gold nanoparticles for bone tissue engineering applications. *Polymers* **2019**, *11* (2), 367.

(33) Cleetus, C. M.; Alvarez Primo, F.; Fregoso, G.; Lalitha Raveendran, N.; Noveron, J. C.; Spencer, C. T.; Ramana, C. V.; Joddar, B. Alginate hydrogels with embedded ZnO nanoparticles for wound healing therapy. *International journal of nanomedicine* **2020**, *15*, 5097−5111.

(34) Theus, A. S.; Ning, L.; Kabboul, G.; Hwang, B.; Tomov, M. L.; LaRock, C. N.; Bauser-Heaton, H.; Mahmoudi, M.; Serpooshan, V. 3D bioprinting of nanoparticle-laden hydrogel scaffolds with enhanced antibacterial and imaging properties. *iScience* **2022**, *25* (9), 104947.

(35) Cengiz, I. F.; Oliveira, J. M.; Reis, R. L. Micro-CT-a digital 3D microstructural voyage into scaffolds: a systematic review of the reported methods and results. *Biomaterials research* **2018**, *22*, 26.

(36) Tuan, H. S.; Hutmacher, D. W. Application of micro CT and computation modeling in bone tissue engineering. *Computer-Aided Design* **2005**, *37* (11), 1151−1161.

(37) Suk, J. S.; Xu, Q.; Kim, N.; Hanes, J.; Ensign, L. M. PEGylation as a strategy for improving nanoparticle-based drug and gene delivery. *Adv. Drug Deliv Rev.* **2016**, *99*, 28−51.

(38) Xu, W.; Jambhulkar, S.; Ravichandran, D.; Zhu, Y.; Kakarla, M.; Nian, Q.; Azeredo, B.; Chen, X.; Jin, K.; Vernon, B.; Lott, D..G; Cornella, J. F.; Shefi, O.; Miquelard-Garnier, G.; Yang, Y.; Song, K. 3D printing-enabled nanoparticle alignment: a review of mechanisms and applications. *Small* **2021**, *17* (45), 2100817.

(39) Yadid, M.; Feiner, R.; Dvir, T. Gold Nanoparticle-Integrated Scaffolds for Tissue Engineering and Regenerative Medicine. *Nano Lett.* **2019**, *19* (4), 2198−2206.

(40) Xu, C.; Tung, G. A.; Sun, S. Size and Concentration Effect of Gold Nanoparticles on X-ray Attenuation As Measured on Computed Tomography. *Chem. Mater.* **2008**, *20* (13), 4167−4169.

(41) Jiang, Z.; Diggle, B.; Tan, M. L.; Viktorova, J.; Bennett, C. W.; Connal, L. A. Extrusion 3D Printing of Polymeric Materials with Advanced Properties. *Advanced Science* **2020**, *7* (17), 2001379.

(42) Boularaoui, S.; Shanti, A.; Lanotte, M.; Luo, S.; Bawazir, S.; Lee, S.; Christoforou, N.; Khan, K. A.; Stefanini, C. Nanocomposite Conductive Bioinks Based on Low-Concentration GelMA and MXene Nanosheets/Gold Nanoparticles Providing Enhanced Printability of Functional Skeletal Muscle Tissues. *ACS Biomaterials Science & Engineering* **2021**, *7* (12), 5810−5822.

(43) Falagan-Lotsch, P.; Grzincic, E. M.; Murphy, C. J. One low-dose exposure of gold nanoparticles induces long-term changes in human cells. *Proc. Natl. Acad. Sci. U. S. A.* **2016**, *113* (47), 13318−13323.